Journal of Materials Chemistry A

Enhanced Thermoelectric Performance in Mg3+xSb1.5Bi0.49Te0.01 via Engineering Microstructure through Melt-Centrifugation

Journal:	*Journal of Materials Chemistry A*
Manuscript ID	TA-ART-10-2020-009993.R2
Article Type:	Paper
Date Submitted by the Author:	12-Dec-2020
Complete List of Authors:	Ozen, Melis; Koc University Graduate School of Sciences and Engineering; Koc University Boron and Advanced Materials Application and Research Center Yahyaoglu, Mujde; Koc University Graduate School of Sciences and Engineering; Koc University Boron and Advanced Materials Application and Research Center Candolfi, Christophe; Institut Jean Lamour, Veremchuk, Igor; Max-Planck-Institut für Chemische Physik fester Stoffe, Kaiser, Felix; Max-Planck-Institut für Chemische Physik fester Stoffe, Chemical Metal Science Burkhardt, Ulrich; MPI CPfS, Chemische Metallkunde Snyder, G.; Northwestern University, Materials Science Grin, Yuri; MPI CPfS, Chemical Metals Science Aydemir, Umut; Koc University Department of Chemistry, Chemistry; Koc University Boron and Advanced Materials Application and Research Center

SCHOLARONE™
Manuscripts

ARTICLE

Enhanced Thermoelectric Performance in $Mg_{3+x}Sb_{1.5}Bi_{0.49}Te_{0.01}$ via Engineering Microstructure through Melt-Centrifugation

Received 00th January 20xx,
Accepted 00th January 20xx

DOI: 10.1039/x0xx00000x

Melis Ozen,[a,b] Mujde Yahyaoglu,[a,b] Christophe Candolfi,[c] Igor Veremchuk,[d] Felix Kaiser,[e] Ulrich Burkhardt,[e] G. Jeffrey Snyder,[f] Yuri Grin,[e] and Umut Aydemir*[b,g]

N-type Zintl phases with earth-abundant and non-toxic constituent elements have attracted intense research interest thanks to their high thermoelectric efficiencies in the mid-temperature range, exemplified by the recently discovered Mg_3Sb_2 material. In this study, the liquid phase is expelled from the microstructure of the optimized *n*-type phase $Mg_{3+x}Sb_{1.5}Bi_{0.49}Te_{0.01}$ by applying a melt-centrifugation technique leading to the formation of lattice dislocations, grain boundary dislocations and increasing porosity. Additional phonon scattering mechanisms were introduced in the microstructure through this manufacturing method, resulting in a significant 50% reduction in the total thermal conductivity from ~1 W m^{-1} K^{-1} to ~0.5 W m^{-1} K^{-1} at 723K. Combined with high power factors, this reduced heat transport leads to a dimensionless thermoelectric figure of merit, *zT*, value of ~1.64 at 723K, 43% higher than the value obtained in untreated $Mg_{3+x}Sb_{1.5}Bi_{0.49}Te_{0.01}$ (*zT* ~1.14 at 723K). This peak *zT* value yields a predicted device *ZT* of 0.95, and a promising theoretical thermoelectric efficiency of about 12%. These results further underline the great potential of the lightweight Mg_3Sb_2 material for mid-temperature energy harvesting via thermoelectric effects.

1. Introduction

Environmental concerns have been continually growing due to dramatic consequences (e.g., air pollution, global warming) of the utilization of non-renewable energy sources such as fossil fuels. Recent studies indicate that beyond 60% of the world's energy is lost mostly as a form of waste heat[1]. Therefore, harvesting waste heat is one of the promising options to support global energy sustainability. Thermoelectric materials, which directly convert heat into electricity or vice-versa, have sparked significant interest in energy generation and refrigeration applications. To improve the conversion efficiency of the thermoelectric devices, the dimensionless thermoelectric figure of merit of the materials, *zT,* defined as $zT = \alpha^2\sigma T/(\kappa_l+\kappa_e)$ should be enhanced. In this formula, α, σ, κ_l, κ_e, and *T* represent the Seebeck coefficient, the electrical conductivity, the lattice thermal conductivity, the electronic thermal conductivity, and the absolute temperature, respectively[2-4]. As these transport properties are interdependent, achieving optimum *zT* values is challenging. Because tuning the electronic transport properties also affects the electronic contribution to the thermal conductivity, it is crucial to reduce the lattice thermal conductivity by phonon scattering without affecting the electronic properties of materials. In recent years, it has been demonstrated that the lattice thermal conductivity can be reduced by atomic scale issues, e.g. increasing complexity of chemical bonding or, on the mesoscale[5], the wide range of phonon frequencies could be scattered by both dislocation scattering and phonon-pore interface scattering[6-9].

Zintl phases can display high thermoelectric efficiencies stemming from their tunable electronic transport properties along with their inherently low lattice thermal conductivities[10-12]. Since their crystal structure is formed by a covalently-bonded network or units of complex anions together with ionically loosely-bonded electropositive cations, Zintl phases may be categorized as phonon-glass, electron-crystal (PGEC) systems [13]. So far, detailed investigations have been focused on various types of Zintl phases such as 0-dimensional (14-1-11)[14, 15], 1-dimensional (5-2-6, 3-1-3)[16, 17], 2-dimensional (9-4-4, 1-2-2, 1-1-4)[18, 19] and 3-dimensional compounds (e.g., clathrates, skutterudites)[20-25]. Among those, several Zintl compounds such as $Yb_{14}MnSb_{11}$[14], $Ca_5Ga_2As_6$[26], β-Zn_4Sb_3[27], $BaGa_2Sb_2$[28, 29] $Yb(Cd_{1-x}Zn_x)Sb_2$[30], $EuZn_2Sb_2$[31] and Mg_3Sb_2[32, 33] were found to be highly-efficient thermoelectric materials upon proper optimization of their carrier concentration. To date, most of the Zintl compounds display persistently *p*-type semiconducting behavior because of intrinsic cation vacancies. However, recent computational studies indicate that *n*-type Zintl phases may

[a] Graduate School of Sciences and Engineering, Koç University, Istanbul-34450, Turkey.
[b] Koç University Boron and Advanced Materials Application and Research Center, Istanbul-34450, Turkey.
[c] Institut Jean Lamour, Université de Lorraine Nancy Cedex-54011, France
[d] Helmholtz-Zentrum Dresden-Rossendorf, Institute of Ion Beam Physics and Materials Research, 01328 Dresden, Germany
[e] Max Planck Institute für Chemische Physik Fester Stoffe, Dresden-01187, Germany.
[f] Department of Materials Science and Engineering, Northwestern University, Evanston, IL-60208, USA
[g] Department of Chemistry, Koç University, Sariyer, Istanbul, 34450, Turkey.
† Footnotes relating to the title and/or authors should appear here.
Electronic Supplementary Information (ESI) available: [details of any supplementary information available should be included here]. See DOI: 10.1039/x0xx00000x

exhibit higher thermoelectric performances compared to their *p*-type counterparts[34-38].

This last prediction has been verified experimentally for the low-cost, non-toxic Mg_3Sb_2 Zintl phase.[39] Mg_3Sb_2 crystallizes in the inverse α-La_2O_3 structure type described in the trigonal space group $P\bar{3}m1$. The crystal structure consists of an anionic $[Mg_2Sb_2]^{2-}$ layer formed by tetrahedrally coordinated Mg with Sb atoms, and an electron donating cationic Mg^{2+} layer at the octahedral sites inserted between two anionic $[Mg_2Sb_2]^{2-}$ units as shown in Fig. 1 [40, 41]. While the $[Mg_2Sb_2]^{2-}$ layers provide high hole mobility, the Mg^{2+} cations are responsible for the good electronic tunability along with low lattice thermal conductivity. We would like to note that Mg_3Sb_2 displays isotropic thermoelectric properties, which Zhang et al. ascribed to three-dimensional bonding network –as opposed to a layer-structure– with the interlayer and intralayer bonds having similar ionic character [38].

Because of Mg's high vapor pressure and reactivity, Mg vacancies that act as electron acceptors are formed during the synthesis steps. The resulting shift of the chemical potential towards the valence bands leads to a *p*-type conduction behaviour[32, 33, 36]. Recently, Tamaki et al. have successfully synthesized *n*-type Mg_3Sb_2 by suppressing the formation of Mg vacancies using an excess amount of Mg in the nominal composition[32]. Remarkably, the subsequent optimization of the thermoelectric properties led to very high zT values ~1.5 near 800 K, outperforming the canonical *p*-type thermoelectric Zintl phase $Yb_{14}MnSb_{11}$. Following this first report, many research groups have devoted enormous attention to further improving the thermoelectric properties of *n*-type Mg_3Sb_2-based materials through various strategies such as band engineering, orbital engineering, scattering mechanism tuning, carrier concentration optimization, annealing under Mg-rich atmosphere, grain size optimization etc.[36, 40-52].

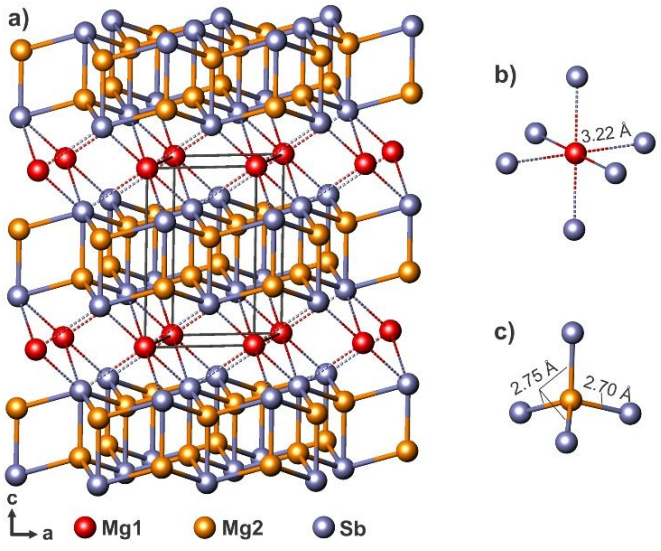

Fig. 1 a) The crystal structure of Mg_3Sb_2 with $[Mg2_2Sb_2]^{2-}$ anionic substructure, $Mg1^{2+}$ cationic sheet and the ionic interaction between them. b) Almost perfect octahedral coordination of Mg1 with six equal Mg1-Sb bonds. c) Slightly distorted tetrahedral coordination of Mg2 with three long and one short Mg2-Sb bonds.

Here, we illustrate the effectiveness of microstructure engineering in refining the thermoelectric properties of *n*-type Mg_3Sb_2, adding a novel strategy to the arsenal mentioned above. This approach is based on squeezing out the excess liquid applying the melt-centrifugation technique, demonstrated for the $(Bi,Sb)_2Te_3$ thermoelectric material[9]. In this study, Pan et al. showed that melt-centrifugation generates lattice and grain boundary dislocations and increases the degree of porosity. Both features open novel sources of phonon scattering, which result in reduced lattice thermal conductivity and hence, increased zT. Herein, the effects of this technique on the microstructure and transport properties of the optimized *n*-type starting composition $Mg_{3.2}Sb_{1.5}Bi_{0.49}Te_{0.01}$ were investigated for the first time. In this study, an excess amount of low-melting element Mg is added to the target composition to achieve eutectic mixtures. Through the centrifugal force, the liquid phase is removed from the microstructure forming dislocation arrays and porosity (See Fig. 2). The best sample displays significantly low lattice thermal conductivity (~0.33 $Wm^{-1}K^{-1}$) with a high zT value of around 1.64 at 723 K, which is higher than that achieved in this study without melt centrifugation (1.14 at 723 K) and other studies reported for $Mg_{3.2}Sb_{1.5}Bi_{0.49}Te_{0.01}$ (zT ~1.5 at 723 K) [32, 34, 53-57].

2. Experimental

2.1. Sample Preparation

High-purity magnesium powder (Mg, 99.8%; Alfa Aesar), bismuth pieces (Bi, 99.999%; Alfa Aesar), antimony shots (Sb, 99.999%; Alfa Aesar) and tellurium pieces (Te, 99.9999%; Alfa Aesar) were used as starting elements. To prevent undesired reactions during high-energy ball milling because of the high reactivity of materials, all sample handling processes were carried out in an Ar-filled glovebox. Stoichiometric mixtures of elements were loaded into a stainless-steel vial with two half-inch stainless-steel balls and sealed in the glove box. The parent compounds with nominal compositions of $Mg_{3.2}Sb_2$ and $Mg_{3.2}Sb_{1.5}Bi_{0.49}Te_{0.01}$ **(MSBT)**, were produced through mechanical alloying for two hours using a high energy mill (SPEX 8000M Mixer/Mill, 1425 rpm). Subsequently, the resulting powders were loaded into a graphite die and consolidated by spark plasma sintering (SPS) for 10 minutes at 873 K under a

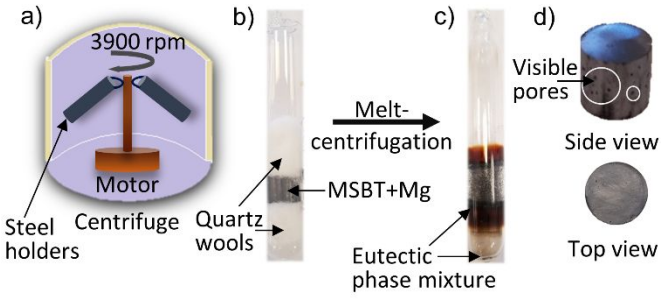

Fig. 2 a) Schematic view of melt-centrifugation apparatus, b) sample in quartz tube before melt-centrifugation, c) sample in quartz tube after melt-centrifugation, d) side and top view of the samples after melt centrifugation process.

This journal is © The Royal Society of Chemistry 20xx

Please do not adjust margins

uniaxial pressure of 50 MPa. For the melt-centrifugation experiments, two different preparation conditions were applied regarding the amount of excess Mg and the way of its addition. For the first case, the raw materials with an excess amount of Mg (46 wt.%) were weighed and added to the vial. The high-energy ball milling was then conducted for 2 h, yielding to the **MSBT_46in_30m_c** sample. For the second case, the main MSBT composition was produced using the above-written route. Afterward, excess amounts of Mg (46 wt.% and 20 wt.%) were **externally** added to 5 g of this pre-reacted sample, and further ball milled for an extra 30 minutes. The same sintering process was applied for this sample. Following SPS, MSBT pellets were sealed under vacuum in a quartz ampoule with quartz wool placed on either side of the pellets (see Fig. 2). Before melt centrifugation, the sample was containing both $Mg_{3+x}Sb_{1.5}Bi_{0.49}Te_{0.01}$ and Mg phases according to the X-ray diffraction pattern (see Sec. 3.1). Afterward, the sealed ampoules were undergone heat treatment at 750°C for two different time periods of 30 minutes and one hour.The heat treatment temperature was selected between the melting points of the Zintl phase and the eutectic point. After the heat treatment, the quartz ampoules were inserted quickly (in ca. 3 seconds) to the centrifuge (Megafuge 8). During the centrifugation process, quartz wools were placed inside the swinging-buckets and the samples were centrifuged for 2 minutes at the speed of 3900 rpm (Fig. 2). Due to the centrifugal force, the randomly distributed liquid phase was squeezed out of the bulk sample to the surface of the quartz ampoules. The as-prepared samples will be hereafter labelled as **MSBT_46ext_30m_c**, **MSBT_20ext_30m_c** and **MSBT_20ext_1h_c**. Labeling the samples with "ext" and "in" indicates the synthesis method used, that is, with external or in-situ Mg addition. The heat treatment durations for the centrifuged samples are indicated as 30m or 1h. Lastly, "c" letter at the end of the labels is used for centrifuged samples.

2.2. Sample Characterization

The crystal structure and the phase purity of the samples were determined by room-temperature X-ray diffraction (XRD, Rigaku Mini Flex 600) with Cu $K_{\alpha1}$ (λ = 1.5406 Å) radiation (40 kV voltage and 15 mA). The lattice parameters were refined, and texture analysis was performed by using the WinCSD program[58]. To analyze the microstructure and the chemical composition, Scanning Electron Microscopy (SEM) with Energy Dispersive X-ray Spectroscopy (EDS) analyses were carried out using a Zeiss Ultra Plus Field Emission Scanning Electron Microscope. SEM images were obtained by etching the surfaces with dilute nitric acid (1 M) for 15 sec. Also, more accurate chemical composition analysis was conducted with wavelength dispersive *X*-ray spectroscopy (WDS) on an electron microprobe (Cameca SX 100, tungsten cathode) using the line compound Mg_2Si and certificated pure elements Sb, Bi and Te as references. . The observation of dislocation arrays and grain boundary dislocations inside the microstructure was performed by Transmission Electron Microscopy (TEM) images using a Hitachi Field Emission Transmission Electron Microscope HF5000 instrument operated at 200 kV. Transmission electron microscope (TEM) images of MSBT sample without melt-centrifugation were recorded on a Hitachi HT7700 TEM instrument operated at 120 kV at Koç University.

2.3. Transport Properties Measurements

All the transport properties were measured between 323 and 723 K. Thermal diffusivity, *D*, was measured on disc-shaped samples (10 mm in diameter) with a Netzsch LFA 467 laser flash apparatus. The thermal conductivity was calculated using the relation $k = D \times C_p \times d$, where C_p is the heat capacity, and *d* is the experimental density. The density of the samples was determined by measuring weight and geometrical dimensions. C_p was calculated by the Maier-Kelley polynomial expression ($C_p = \frac{3NR}{M_w}(1 + 1.3 \times 10^{-4}T - 4 \times 10^{3}T^{-2})$, between 323 and 723 K (See Fig. S1) [59, 60]. The electronic thermal conductivity κ_e was calculated through the Wiedemann-Franz law $\kappa_e = L\sigma T$, where *L* is the Lorenz number and σ is the electrical conductivity. The Lorenz numbers were calculated for each sample through the relation, $\frac{L}{10^{-8}W\Omega K^{-2}} = 1.5 + \exp\left(\frac{-|\alpha|}{116\mu V/K}\right)$, where α is measured in μV/K [61].

Seebeck coefficient and electrical resistivity measurements were performed using an ULVAC ZEM-3 system. For these measurements, samples were cut into rectangular bars using a low-speed diamond-wire saw (MTI-SYJ-150). Of note, the LFA and ZEM-3 measurements were all performed parallel to the SPS pressing direction.

The thermoelectric device figure of merit, *ZT*, value and the maximum efficiency, η, were calculated by using a spreadsheet supplied in the study of Snyder et al.[62] Basically, *ZT* value for a specific temperature difference $\boldsymbol{\Delta T = T_h - T_c}$ was calculated with $\boldsymbol{ZT = \left(\frac{T_h - T_c(1-\eta)}{T_h(1-\eta) - T_c}\right)^2}$ by using maximum efficiency, η, determined between hot and cold side temperatures through temperature-dependent *S(T)*, *ρ(T)*, and *κ(T)*. For further details, see Ref. 62. The uncertainties are considered to be in the range of 5 - 10 % in resistivity, Seebeck coefficient, and thermal diffusivity measurements. The combined uncertainty in zT values may reach up to 15-20 % [63, 64].

3. Results and Discussion

3.1. Phase and Crystal Structure Analysis

As depicted in the phase diagram of Mg_3Sb_2 (Fig. S2), Mg excess phase (65 at-% Mg) melts around 750°C (eutectic temperature ~627°C) and dissolves a small amount of $Mg_{3+x}Sb_{1.5}Bi_{0.49}Te_{0.01}$. During the melt centrifugation, a fraction of the liquid phase is removed from the bulk sample through the walls of the quartz ampoule, and almost phase-pure and porous $Mg_{3+x}Sb_{1.5}Bi_{0.49}Te_{0.01}$ can be obtained. Fig. 3 presents the XRD results of the SPS treated samples $Mg_{3+x}Sb_2$, MSBT, MSBT_20ext_1h and MSBT_20ext_1h_c. For all samples, the

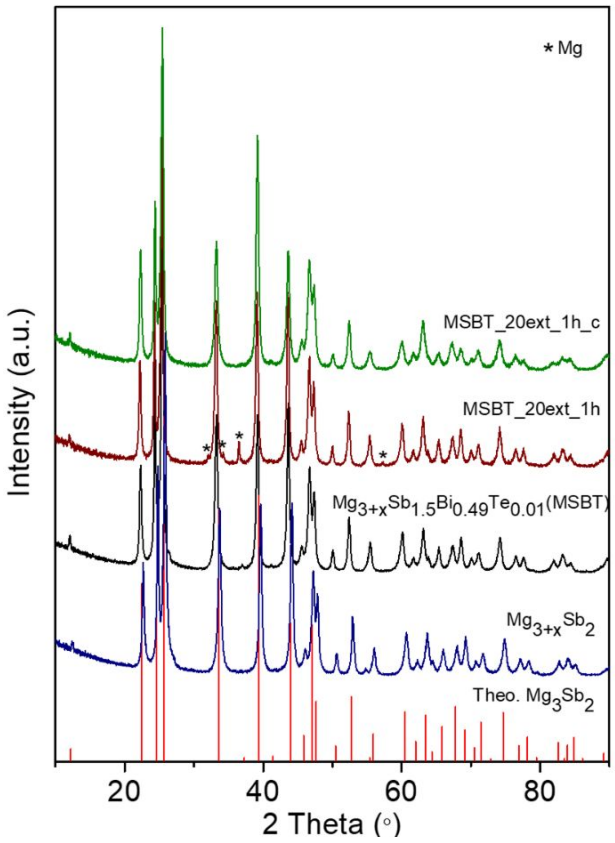

Fig. 3 XRD patterns (Cu-$K_{\alpha 1}$ radiation) of $Mg_{3+x}Sb_2$, MSBT (black), MSBT_20ext_1h (pink) and MSBT_20ext_1h_c (green).

reflections of the main phase can be well indexed by the trigonal Mg_3Sb_2 crystal structure ($P\bar{3}m1$ space group). XRD measurements demonstrate that $Mg_{3+x}Sb_{1.5}Bi_{0.49}Te_{0.01}$ (MSBT) was produced as a pure phase. The sample MSBT_20ext_1h shows additional reflections that correspond to elemental Mg. After the centrifugation process, only the Zintl phase was observed within the detection limits of XRD. The rest of the centrifuged samples also displayed similar results with the MSBT_20ext_1h sample before and after the centrifugation process (See Fig. S3). The EDS elemental mapping analyses performed on MSBT_20ext_30m_c and MSBT_20ext_1h_c samples show Mg and Bi excess grains within the microstructure (see Fig. S4).

The refined lattice parameters of the samples are tabulated in Table S1. The MSBT sample has lattice parameters very similar to those published for single-crystalline Mg_3Sb_2[65]. The substitution of Bi^{3-} for Sb^{3-} leads to slightly higher lattice parameters for the MSBT sample due to the larger ionic radii of Bi^{3-} (1·93 Å) compared to Sb^{3-} (1·88 Å)[66]. After applying centrifugation followed by 30 and 60 min of annealing, the lattice parameters were increased slightly, suggesting a tiny change in the sample's chemical composition. Based on the Rietveld refinements conducted on MSBT_20ext_1h and MSBT_20ext_1h_c samples, no pronounced texturing was observed for both samples (See Fig. S5 and S6). This agrees with the theoretical calculations demonstrating Mg_3Sb_2 has isotropic chemical bonding and transport properties[38, 67, 68]. The experimental studies carried out by Imasato et al., Tamaki et al., and Xin et al. manifest that Mg_3Sb_2 displays isotropic thermal conductivity behavior, while the experimental electronic transport data given by Song et al. and Lv et al. show that there is no reasonable difference in transport properties measured in different directions[32, 65, 69-71].

The composition of the MSBT was determined by WDXS analysis by averaging the results of 10 different, randomly-chosen spots as $Mg_{3.08(1)}Sb_{1.44(2)}Bi_{0.47(1)}Te_{0.01(3)}$, which points to similar stoichiometry as the nominal composition (SI Table S2 and Fig. S7).

3.2. Microstructure Analysis

Microstructure examinations were performed by SEM and TEM. Several TEM studies have been previously conducted on Mg_3Sb_2-based materials synthesized by mechanical alloying [51, 54, 72-74]. To the best of our knowledge, none of the studied samples present lattice dislocations or ordered grain boundaries in the microstructures. TEM images shown in Fig. 4 for MSBT sample indicate that mechanical alloying technique without additional synthetic treatments (e.g., melt centrifugation) does not tend to form lattice dislocations or ordered grain boundaries. In Fig. 5a and 5b, SEM images of the samples MSBT_20ext_30m_c and MSBT_20ext_1h_c show that porosities with various sizes emerged after the centrifugation process. Therefore, to further investigate the microstructural effects of melt-centrifugation, TEM images of MSBT_20ext_30m_c are shown from two different perspectives, one from out-of-plane direction (Fig. 5c; parallel to the sintering direction) and the other from the in-plane direction (Fig. 5d; perpendicular to the sintering direction). Distinctly ordered grain boundary dislocations were observed from both in-plane and out-of-plane directions owing to the centrifugal force (For large and more distinct images see Fig. S8). Besides, lattice dislocations and dislocation arrays within the grains were identified in both directions. The removal of the

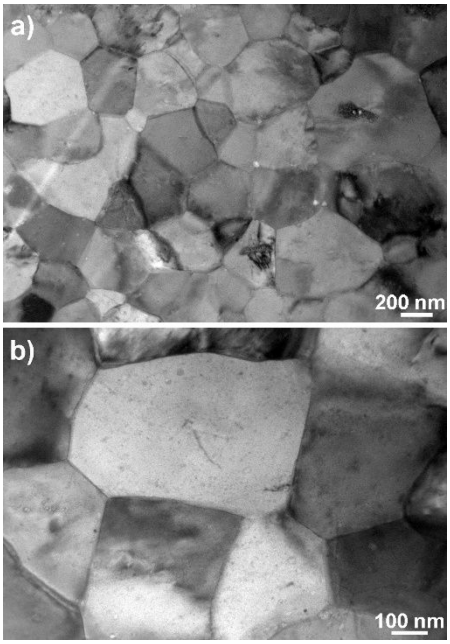

Fig. 4 TEM images of MSBT sample ($Mg_{3+x}Sb_{1.5}Bi_{0.49}Te_{0.01}$) without melt-centrifugation.

This journal is © The Royal Society of Chemistry 20xx

Please do not adjust margins

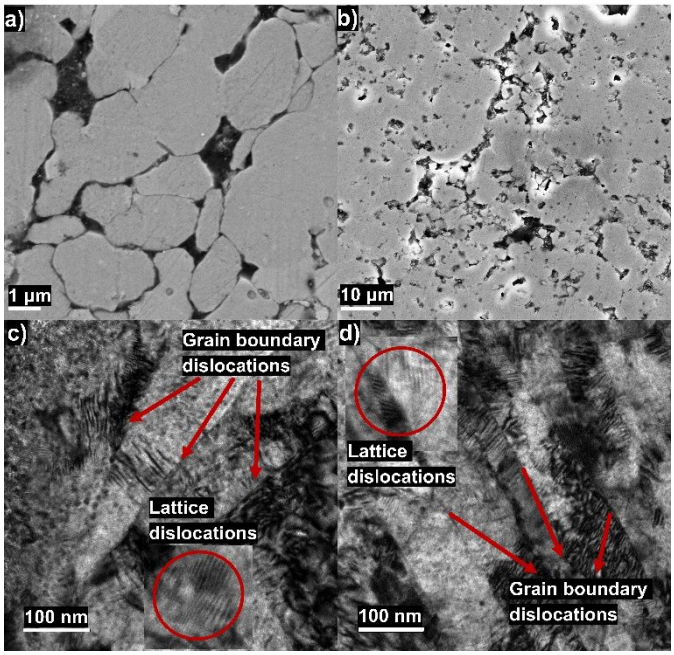

Fig. 5 SE (Secondary Electron) images (5 kV and 20 kV HV) of melt-centrifuged samples a) MSBT_20ext_30m_c b) MSBT_20ext_1h_c, and TEM images of MSBT_20ext_30m_c c) taken from out-plane direction and d) taken from in-plane direction

liquid eutectic phase under strong centrifugal force induces grain rotations and misfits in the microstructure. These large grain misfits are accommodated by the formation of lattice dislocations. In addition, during the uniaxial melt centrifugation, liquid eutectic phase penetrates through the grain boundaries resulting in much higher diffusion length for the atoms and the dislocations at the grain boundaries. This effect is considered as the main reason for the formation of ordered grain boundaries. As dislocations generate strain fields and act as an additional source of phonon diffusion, their presence may prevent phonon propagation and reduce the lattice thermal conductivity[6, 9, 75, 76].

3.3. Electronic Transport

As shown by Imasato et. al. and Shuai et. al., the excess Mg in $Mg_{3+x}Sb_{1.5}Bi_{0.49}Te_{0.01}$ can deteriorate the electronic transport properties[54, 55]. The addition of 46 wt.% excess amount of Mg decreases the electrical resistivity values, due to the additional electrons provided. The electrical resistivity values of the sample with an external addition of the same amount of Mg (MSBT_46ext_30m_c) are similar to those of the non-centrifuged sample. This lack of difference might be related to lower Mg concentration in the crystal structure comparing with internally Mg added samples, suggesting that the external addition facilitates the removal of excess Mg.

By decreasing the excess amount of Mg from 46 wt.% to 20 wt.%, the electrical resistivity increases substantially after centrifugation. Both the formation of porosity and the lower amount of Mg might explain this behavior. As observed in Fig. 6a, increasing the heat treatment time from 30 min to 1h leads

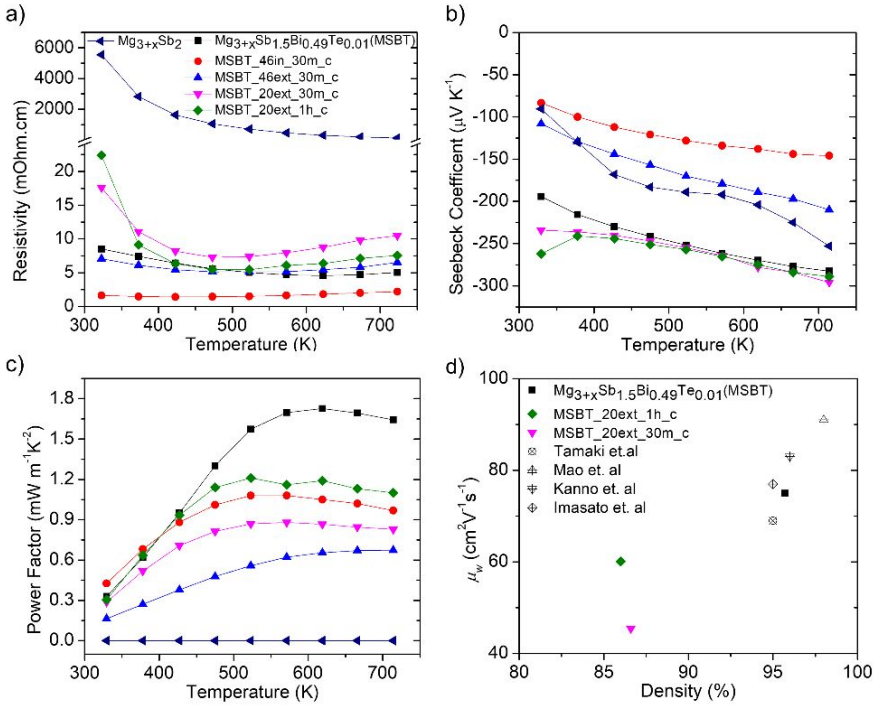

Fig. 6 a)The electrical resistivity, b) Seebeck coefficient of $Mg_{3+x}Sb_2$, MSBT(black), MSBT_46in_30m_c (red), MSBT_46ext_30m_c (blue), MSBT_20ext_30m_c (pink) and MSBT_20ext_1h_c (green) as a function of temperature, c) weighted mobility data as a function of temperature and d) weighted mobility as a function of density data of MSBT_20ext_30m_c (pink) and MSBT_20ext_1h_c (green) compared to the literature data [32, 46, 55, 57].

to a decrease in the electrical resistivity for the sample MSBT_20ext_1h_c compared to MSBT_20ext_30m_c. This behavior is likely associated with grain-boundary dominated charge transport. As grains act as two different phases at the grain boundaries, a potential barrier is generated along the grain boundary resulting in higher electrical resistivity[43, 48]. As shown in Fig. S9, different heat treatments lead to different microstructural features. When the annealing time is increased from 30 min. to 1 h, the removal of the liquid phase from the microstructure through centrifugation results in more homogeneously-distributed porosity for MSBT_20ext_1h_c compared to MSBT_20ext_30m_c sample. In addition, Fig. S10 highlights the differences between the grain structure of these samples. While MSBT_20ext_30m_c sample has almost well-defined grain boundaries, MSBT_20ext_1h_c sample demonstrates more fused grains and semicoherent grain boundaries as shown by residual neck formation. As discussed by Kim et al., semicoherent grain boundaries have less of an effect on electron scattering while inducing enough strain for significant phonon scattering[6]. Therefore, the presence of semicoherent grain boundaries explains the higher mobility and lower electrical resistivity in the MSBT_20ext_1h_c sample compared to MSBT_20ext_30m_c sample.

The negative sign of the Seebeck coefficient evidences that all samples exhibit *n*-type behavior remaining unchanged even after centrifugation processes (Fig. 6b). Both the MSBT_46in_30m_c and MSBT_46ext_30m_c samples have very low Seebeck coefficients compared to the reference compound $Mg_{3+x}Sb_{1.5}Bi_{0.49}Te_{0.01}$(MSBT). These results are in accord with the trend observed in the electrical resistivity values, indicative of significant variations in the electron concentration resulting from the excess Mg, which is retained in the crystal structure. On the other hand, with 20 wt.% Mg addition, the Seebeck coefficients of MSBT_20ext_1h_c and MSBT_20ext_30m_c are almost identical to that of the non-centrifuged MSBT sample at higher temperatures. Large, negative Seebeck coefficients observed for those. The high-temperature heat treatment applied before centrifugation might result in Te loss along with Mg. However, due to the very small amount of Te in the composition, it is hard to detect this change by chemical analyses. Besides, the similar Seebeck coefficients of the MSBT_20ext_1h_c and MSBT_20ext_30m_c samples promote the idea that the difference observed in the ρ values are due to grain-boundary-dominated charge transport, in which its influence on the Seebeck coefficient is negligible.

The weighted mobilities of the samples were calculated from the measured electrical conductivity and Seebeck coefficient data using a Drude–Sommerfeld free electron model approximation[77]. The weighted mobility is independent of the position of the chemical potential and hence, of the carrier concentration. It provides valuable information about the power factor as well as *zT*, provided that the carrier concentration is optimized, and about the intrinsic properties of the charge carriers, grain boundary resistance, charge transport mechanisms with more accurate temperature dependence [43, 77]. The weighted mobility values of centrifuged samples are reported in Fig. S11. Compared to the estimated weighted mobility data counting the grain boundary resistance and bipolar effects (See Ref. 43), the weighted mobilities of the centrifuged samples are more affected by the grain boundary resistance[77]. Therefore, the weighted mobility values of the MSBT_20ext_1h_c and MSBT_20ext_30m_c samples are presented in Fig. 6d at 573K to eliminate this effect. The relatively low weighted mobility values compared to MSBT sample and the literature might arise from the low average distance between the scattering centers, which are analogous to the electron mean free path[78]. Also, the lower density (86.6% and 85.3%) of MSBT_20ext_1h_c and MSBT_20ext_30m_c that emerged in the microstructure due to the porosities results in significantly low weighted mobilities; being in an agreement with the study conducted by Witting et. al[79]. As seen in Fig. 6d, increasing the annealing time suppresses the negative effect of the scattering centers which mentioned in the electrical resistivity discussion, leading to higher weighted mobility values.

3.4. Thermal Transport

The total thermal conductivity κ of the different samples is presented in Fig. 7a. The lattice thermal conductivity values κ_l, shown in Fig. 7b, were obtained by subtracting κ_e from κ. Despite the decrease in the density of the MSBT_46in_30m_c sample, κ is higher at high temperature. This behavior is related to minority carrier effects that result in an additional bipolar contribution to κ. In line with the electrical resistivity and Seebeck coefficient data, the κ_e values of MSBT_46in_30m_c increase with increasing temperature much faster than the concomitant decrease in κ_l. For the samples MSBT_20ext_1h_c and MSBT_20ext_30m_c, κ_e was not affected significantly by the centrifugation process (See Fig. S12). In contrast, as seen in

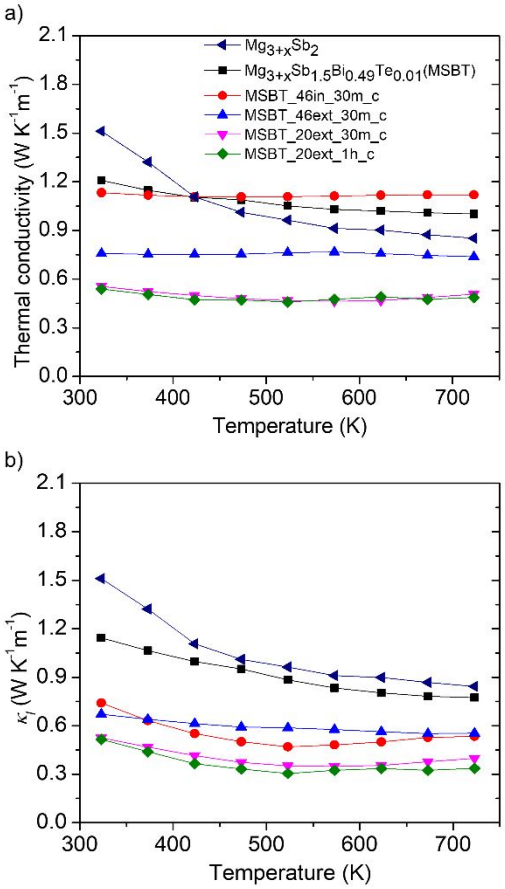

Fig. 7 a) Thermal conductivity and b) lattice thermal conductivity of $Mg_{3+x}Sb_2$, MSBT(black), MSBT_46in_30m_c (red), MSBT_46ext_30m_c, MSBT_20ext_30m_c (pink) and MSBT_20ext_1h_c (green) $Mg_{3+x}Sb_{1.5}Bi_{0.49}Te_{0.01}$ samples as a function of temperature

Please do not a

Fig. 5 and Fig. S8, grain boundary and lattice dislocations impede the propagation of phonons and result in a significant decrease in κ_l as high as 56-60% (Fig. 7b). This behavior is analogous with the melt-centrifugation study on $Bi_{0.3}Sb_{1.7}Te_3$, in which a reduction in κ_l of around 60% was reported due to the formation of pores, dislocation strains, and interfaces. The effects of two different phases (air in pores and the main Mg_3Sb_2 phase) on the thermal conductivity has been analyzed using the effective medium theory (EMT) with the relation $\boldsymbol{\kappa_{l,p} = \kappa_{l,d} f_\kappa(\varepsilon)}$, where $\boldsymbol{f_\kappa(\varepsilon) = (1 - 3\varepsilon/2)}$ and ε is the volume fraction of porosity[9]. Using porosity of centrifuged samples of ε □0.14, EMT results in a $\boldsymbol{\kappa_{l,p}/\kappa_{l,d}}$ of around 0.78, indicating that the porous structure leads to □22% reduction in lattice thermal conductivity, with the extra reduction stemming from other phonon scattering mechanisms, e.g., dislocation strain scattering. Compared with the measured lattice thermal conductivity data from the literature, MSBT_20ext_1h_c and MSBT_20ext_30m_c present very low lattice thermal conductivity (0.50 to 0.33 $Wm^{-1}K^{-1}$ between 323-723 K) and total thermal conductivity (0.55 to 0.48 $Wm^{-1}K^{-1}$ between 323-723 K) for all temperature range, with a remarkable difference of around 38-50 % [32, 34, 46, 52, 54-57].

While the defects and grain boundaries in the microstructure are detrimental to the electrical conduction, different types of dislocations and porosity formation additionally diminish the thermal conductivity by creating phonon scattering mechanisms covering a broader frequency range of the phonon spectrum. This beneficial influence becomes more apparent for the MSBT_20ext_1h_c and MSBT_20ext_30m_c samples. As discussed for the electrical transport properties of these samples, MSBT_20ext_30m_c shows higher electrical resistivity values than MSBT_20ext_1h_c does; likewise, the electronic thermal conductivity values of them are similar. The comparison of these two samples, one annealed for 30 min. and the other one for 1 hour, reveals a homogenous distribution of porosity in the latter case (Fig. S9a and S9c). This behavior can be also correlated to semicoherent grain boundaries observed in MSBT_20ext_1h_c (Fig. S10) for higher temperature and annealing time, implying that, although the chemical composition did not change appreciably, the distance between the scattering centers have increased for the latter sample. Therefore, a decrease in the electrical resistivity and an increase in weighted mobility are observed for this sample. This led to slightly higher κ_e value for MSBT_20ext_1h_c , which was compensated by lower κ_l as a consequence of the porosity difference(volume fraction of 13.5% vs 14.7%). Finally, compared to the MSBT sample without centrifugation, lower electronic thermal conductivity combines with stronger phonon scattering, resulting in total thermal conductivity values that decrease by more than 50% for centrifuged samples, as illustrated in Fig. 7a.

3.5. Thermoelectric Figure of Merit

Fig. 8a shows the temperature dependence of the thermoelectric figure of merit *zT* for centrifuged and non-centrifuged samples. The results evidence that the addition of 46 wt.% Mg negatively affects the *zT* values for both in-situ and external addition to the main composition. On the other hand, an addition of only 20 wt.% Mg successfully augments the *zT* values over the entire temperature range with respect to $Mg_{3+x}Sb_{1.5}Bi_{0.49}Te_{0.01}$. The dramatic reduction in thermal conductivity is the main ingredient yielding higher *zT* values. Higher *zT* is directly correlated with a higher quality factor, $B \propto \mu_w / \kappa_l$; for this reason, higher weighted mobility is needed for an efficient thermoelectric material together with low lattice thermal conductivity [40, 43]. As mentioned above, the presence of different scattering mechanisms due to the peculiar microstructure affects both the thermal and electronic properties. In this regard, quality factor determination is essential to assess the net gain from melt-centrifugation, independently from variations in the carrier concentration. The comparison of the quality factors of MSBT sample (B = 0.5) and the centrifuged ones, MSBT_20ext_30m_c (B = 0.56), and MSBT_20ext_1h_c (B = 0.83) at 723 K, evidences a clear effect of melt-centrifugation. Although the MSBT sample has a higher weighted mobility value, the centrifuged samples present

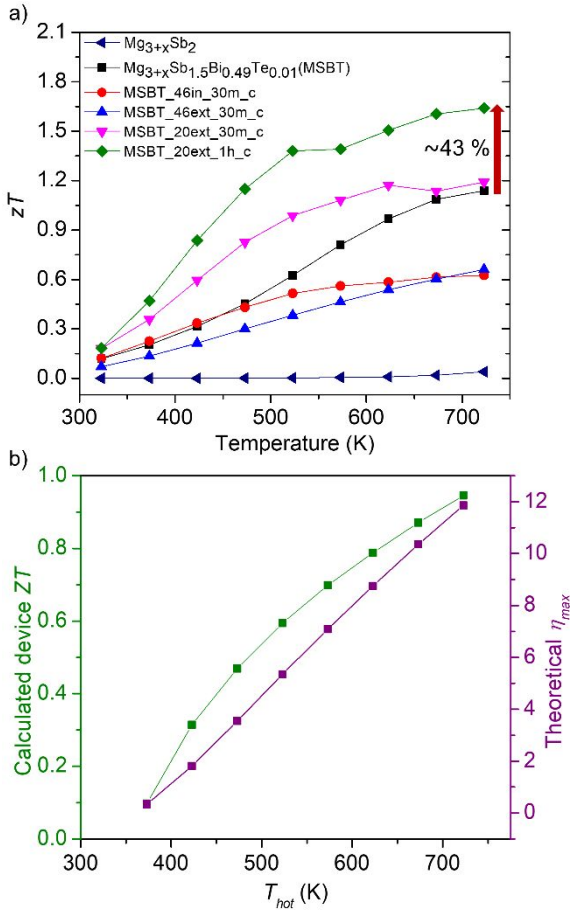

Fig. 8 a) The thermoelectric figure of merit of $Mg_{3+x}Sb_2$, MSBT (black), MSBT_46in_30m_c (red), MSBT_46ext_30m_c, MSBT_20ext_30m_c (pink) and MSBT_20ext_1h_c (green) samples as a function of temperature. b) Calculated device *ZT* and calculated theoretical maximum efficiency of MSBT_20ext_1h_c (green)

higher quality factors due to much lower κ_l values achieved. This may indicate that pore-interface and dislocation scattering is more effective in reducing thermal conductivity than electrical conductivity because of larger mean free paths of phonons compared to those of the charge carriers. With such hierarchical microstructure comprising semicoherent grain boundaries, an overall enhancement in *zT* for the melt-centrifuged samples is achieved[9]. With longer heat treatment times and centrifugation, a peak *zT* of ~1.64 was achieved for this sample, corresponding to an enhancement of around 43% compared to that of the MSBT sample without applying any carrier concentration optimization method. Moreover, the highest *zT* achieved in this study is nearly 10 % higher than those reported for *n*-type $Mg_{3.2}Sb_{1.5}Bi_{0.49}Te_{0.01}$ (nominal composition) with *zT* of ~1.5[32, 34, 53-57] at 723 K, and comparable to the best-reported *zT* values achieved with different doping strategies (Fig. 9)[55-57, 74]. DSC/TG experiments performed on MSBT_20ext_30m sample up to 725 K reveals no weight loss (Fig. S13) along with no endothermic or exothermic effect, pointing out relative stability of this melt-centrifuged material. A cyclic transport data for the same sample (Fig. S14) shows strong hysteresis for the resistivity data at low temperatures, which does not dramatically change the sample's overall thermoelectric performance at higher temperatures. The hysteresis in the resistivity data is significantly reduced during the second cycle. This behavior can be attributed to the reduction of highly resistive grain boundaries and their resistance due to partial grain growth during the first heating cycle. In a separate study[44], annealing an MSBT sample under Mg vapor was reported to increase the grain size and reduce the grain boundary scattering. This led to significant enhancement in the electron mobility (improving low-temperature electrical conductivity) with negligible change in the Seebeck values and thermal conductivity, similarly found in our case.

As depicted in Fig 8b, the device *ZT* value of the best-performing sample (MSBT_20ext_1h_c) was calculated to be 0.95 at 723 K, which corresponds to a theoretical maximum efficiency value of around 12 %.

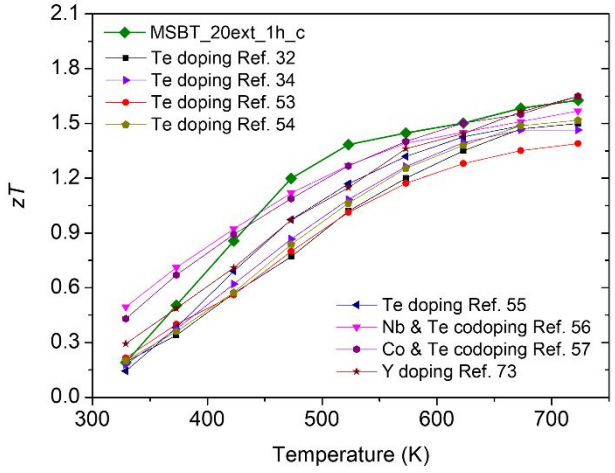

Fig. 9 Temperature-dependent *zT* values of MSBT_20ext_1h_c within the temperature range 323 – 723 K in comparison with those reported for other *n*-type Mg_3Sb_2 samples.

4. Conclusions

A microstructure engineering strategy based on melt-centrifugation was successfully implemented to the *n*-type Zintl phase $Mg_{3+x}Sb_{1.5}Bi_{0.49}Te_{0.01}$ for the first time. This technique not only creates lattice and grain boundary dislocations but also a porous microstructure. By annealing at 750°C for one hour before the melt centrifugation, the electronic transport properties of the MSBT_20ext_1h_c sample were enhanced compared to those of the MSBT_20ext_30m_c sample annealed for only 30 minutes. As a result, although the power factor decreased by ~30% compared to noncentrifuged sample, a marked drop in the thermal conductivity of around 50% led to enhanced *zT* values thanks to melt-centrifugation. The total thermal conductivity was reduced by 50 % from 1 W m^{-1} K^{-1} to ~0.5 W m^{-1} K^{-1} at 723 K for the MSBT_20ext_1h_c sample. Additionally, the samples MSBT_20ext_1h_c and MSBT_20ext_30m_c display increased *zT* values over the entire temperature range. Regarding the MSBT_20ext_1h_c sample, the highest *zT* value increases from 1.14 to 1.64 at 723K which signifies an enhancement of almost 43%. The hierarchical microstructure and well-fused grains lead to an overall enhancement in *zT* for the melt-centrifuged samples. Besides, with a calculated device *ZT* value of 0.95, a promising theoretical efficiency of approximately 12% is predicted for this sample (Fig 7b.). Our results further underline the strong potential of the lightweight Zintl phase Mg_3Sb_2 for mid-temperature thermoelectric applications in power generation. This work elaborately demonstrates that high thermoelectric efficiency can be achieved in porous, lightweight thermoelectric materials through the melt-centrifugation technique.

Acknowledgments

This work is supported financially by The Scientific and Technological Research Council of Turkey with project numbers 218M254. U.A. and C.C. acknowledge the financial support of the French Agence Nationale de la Recherche (ANR), through the PRCI project DENZIP (ANR-18-CE05-0042). The authors acknowledge the Max-Planck Institute für Chemische Physik Fester Stoffe for the access to their instruments for the sintering experiments and WDXS analyses performed in this study. U.A. acknowledges Barış Yağcı and other researchers at Koç University Surface Science and Technology Center for SEM measurements. U.A. would also like to thank Burak Bayram and Gülcan Çorapcıoğlu at Koç University for the TEM measurements. G.J.S. acknowledges the support of award 70NANB19H005 from NIST as part of the Center for Hierarchical Materials Design (CHiMaD).

Conflicts of interest

There are no conflicts to declare.

This journal is © The Royal Society of Chemistry 20xx

Please do not adjust margins

Notes and references

1. C. Forman, I. K. Muritala, R. Pardemann and B. Meyer, *Renewable and Sustainable Energy Reviews*, 2016, **57**, 1568-1579.
2. X. Zhou, Y. Yan, X. Lu, H. Zhu, X. Han, G. Chen and Z. Ren, *Materials Today*, 2018, **21**, 974-988.
3. W. Liu, J. Hu, S. Zhang, M. Deng, C.-G. Han and Y. Liu, *Materials Today Physics*, 2017, **1**, 50-60.
4. G. Tan, L.-D. Zhao and M. G. Kanatzidis, *Chemical reviews*, 2016, **116**, 12123-12149.
5. Y. Grin, *Journal of Solid State Chemistry*, 2019, **274**, 329-336.
6. S. I. Kim, K. H. Lee, H. A. Mun, H. S. Kim, S. W. Hwang, J. W. Roh, D. J. Yang, W. H. Shin, X. S. Li and Y. H. Lee, *Science*, 2015, **348**, 109-114.
7. Z. Chen, B. Ge, W. Li, S. Lin, J. Shen, Y. Chang, R. Hanus, G. J. Snyder and Y. Pei, *Nature communications*, 2017, **8**, 13828.
8. H. Zhao, B. Cao, S. Li, N. Liu, J. Shen, S. Li, J. Jian, L. Gu, Y. Pei and G. J. Snyder, *Advanced Energy Materials*, 2017, **7**, 1700446.
9. Y. Pan, U. Aydemir, J. A. Grovogui, I. T. Witting, R. Hanus, Y. Xu, J. Wu, C. F. Wu, F. H. Sun and H. L. Zhuang, *Advanced Materials*, 2018, **30**, 1802016.
10. E. S. Toberer, C. A. Cox, S. R. Brown, T. Ikeda, A. F. May, S. M. Kauzlarich and G. J. Snyder, *Advanced Functional Materials*, 2008, **18**, 2795-2800.
11. S. R. Brown, E. S. Toberer, T. Ikeda, C. A. Cox, F. Gascoin, S. M. Kauzlarich and G. J. Snyder, *Chemistry of Materials*, 2008, **20**, 3412-3419.
12. O. Janka and S. M. Kauzlarich, *Encyclopedia of Inorganic and Bioinorganic Chemistry*, 2011, 1-14.
13. S. M. Kauzlarich, S. R. Brown and G. J. Snyder, *Dalton Transactions*, 2007, 2099-2107.
14. S. R. Brown, S. M. Kauzlarich, F. Gascoin and G. J. Snyder, *Chemistry of materials*, 2006, **18**, 1873-1877.
15. C. Uher, *Materials aspect of thermoelectricity*, CRC press, 2016.
16. S. Chanakian, U. Aydemir, A. Zevalkink, Z. M. Gibbs, J.-P. Fleurial, S. Bux and G. J. Snyder, *Journal of Materials Chemistry C*, 2015, **3**, 10518-10524.
17. S. Ohno, A. Zevalkink, Y. Takagiwa, S. K. Bux and G. J. Snyder, *Journal of Materials Chemistry A*, 2014, **2**, 7478-7483.
18. G. S. Pomrehn, A. Zevalkink, W. G. Zeier, A. Van De Walle and G. J. Snyder, *Angewandte Chemie International Edition*, 2014, **53**, 3422-3426.
19. A. Bhardwaj and D. Misra, *Rsc Advances*, 2014, **4**, 34552-34560.
20. H. Zhang, H. Borrmann, N. Oeschler, C. Candolfi, W. Schnelle, M. Schmidt, U. Burkhardt, M. Baitinger, J.-T. Zhao and Y. Grin, *Inorganic chemistry*, 2011, **50**, 1250-1257.
21. C. Uher, in *Semiconductors and semimetals*, Elsevier, 2001, vol. 69, pp. 139-253.
22. C. Candolfi, B. Lenoir, A. Dauscher, B. Malaman, E. Guilmeau, J. Hejtmanek and J. Tobola, *Applied Physics Letters*, 2010, **96**, 262103.
23. Y. Tang, Y. Qiu, L. Xi, X. Shi, W. Zhang, L. Chen, S.-M. Tseng, S.-w. Chen and G. J. Snyder, *Energy & Environmental Science*, 2014, **7**, 812-819.
24. X. Shi, Y. Pei, G. J. Snyder and L. Chen, *Energy & environmental science*, 2011, **4**, 4086-4095.
25. J. Shuai, J. Mao, S. Song, Q. Zhang, G. Chen and Z. Ren, *Materials Today Physics*, 2017, **1**, 74-95.
26. Y. L. Yan, Y. X. Wang and G. B. Zhang, *Journal of Materials Chemistry*, 2012, **22**, 20284-20290.
27. E. S. Toberer, P. Rauwel, S. Gariel, J. Taftø and G. J. Snyder, *Journal of materials chemistry*, 2010, **20**, 9877-9885.
28. U. Aydemir, A. Zevalkink, A. Ormeci, Z. M. Gibbs, S. Bux and G. J. Snyder, *Chemistry of Materials*, 2015, **27**, 1622-1630.
29. U. Aydemir, A. Zevalkink, A. Ormeci, S. Bux and G. J. Snyder, *Journal of Materials Chemistry A*, 2016, **4**, 1867-1875.
30. X.-J. Wang, M.-B. Tang, H.-H. Chen, X.-X. Yang, J.-T. Zhao, U. Burkhardt and Y. Grin, *Applied Physics Letters*, 2009, **94**, 092106.
31. H. Zhang, J.-T. Zhao, Y. Grin, X.-J. Wang, M.-B. Tang, Z.-Y. Man, H.-H. Chen and X.-X. Yang, *The Journal of chemical physics*, 2008, **129**, 164713.
32. H. Tamaki, H. K. Sato and T. Kanno, *Advanced Materials*, 2016, **28**, 10182-10187.
33. C. L. Condron, S. M. Kauzlarich, F. Gascoin and G. J. Snyder, *Journal of Solid State Chemistry*, 2006, **179**, 2252-2257.
34. S. Ohno, K. Imasato, S. Anand, H. Tamaki, S. D. Kang, P. Gorai, H. K. Sato, E. S. Toberer, T. Kanno and G. J. Snyder, *Joule*, 2018, **2**, 141-154.
35. P. Gorai, E. S. Toberer and V. Stevanović, *Journal of Applied Physics*, 2019, **125**, 025105.
36. B. R. Ortiz, P. Gorai, L. Krishna, R. Mow, A. Lopez, R. McKinney, V. Stevanović and E. S. Toberer, *Journal of Materials Chemistry A*, 2017, **5**, 4036-4046.
37. P. Gorai, B. R. Ortiz, E. S. Toberer and V. Stevanović, *Journal of Materials Chemistry A*, 2018, **6**, 13806-13815.
38. J. Zhang, L. Song and B. B. Iversen, *Npj Computational Materials*, 2019, **5**, 76.
39. X. Tan, G.-Q. Liu, H. Hu, H. Shao, J. Xu and J. Jiang, *Journal of Materials Chemistry A*, 2019, **7**, 8922-8928.
40. J. He and T. M. Tritt, *Science*, 2017, **357**, eaak9997.
41. X. Sun, X. Li, J. Yang, J. Xi, R. Nelson, C. Ertural, R. Dronskowski, W. Liu, G. J. Snyder and D. J. Singh, *Journal of computational chemistry*, 2019, **40**, 1693-1700.
42. B. Xu, R. Li, G. Yu, S. Ma, Y. Wang, Y. Wang and L. Yi, *Journal of the Physical Society of Japan*, 2017, **86**, 024601.
43. K. Imasato, S. D. Kang and G. J. Snyder, *Energy & Environmental Science*, 2019, **12**, 965-971.
44. M. Wood, J. J. Kuo, K. Imasato and G. J. Snyder, *Advanced Materials*, 2019, **31**, 1902337.
45. K. Imasato, C. Fu, Y. Pan, M. Wood, J. J. Kuo, C. Felser and G. J. Snyder, *Advanced Materials*, 2020, 1908218.
46. T. Kanno, H. Tamaki, H. K. Sato, S. D. Kang, S. Ohno, K. Imasato, J. J. Kuo, G. J. Snyder and Y. Miyazaki, *Applied Physics Letters*, 2018, **112**, 033903.
47. K. Imasato, M. Wood, J. J. Kuo and G. J. Snyder, *Journal of Materials Chemistry A*, 2018, **6**, 19941-19946.
48. J. J. Kuo, S. D. Kang, K. Imasato, H. Tamaki, S. Ohno, T. Kanno and G. J. Snyder, *Energy & Environmental Science*, 2018, **11**, 429-434.
49. K. Imasato, S. D. Kang, S. Ohno and G. J. Snyder, *Materials Horizons*, 2018, **5**, 59-64.
50. J. Zhang, L. Song, G. K. Madsen, K. F. Fischer, W. Zhang, X. Shi and B. B. Iversen, *Nature communications*, 2016, **7**, 10892.

51. J. Zhang, L. Song, A. Mamakhel, M. R. V. Jørgensen and B. B. Iversen, *Chemistry of Materials*, 2017, **29**, 5371-5383.
52. J. Zhang, L. Song, S. H. Pedersen, H. Yin, L. T. Hung and B. B. Iversen, *Nature communications*, 2017, **8**, 13901.
53. X. Chen, H. Wu, J. Cui, Y. Xiao, Y. Zhang, J. He, Y. Chen, J. Cao, W. Cai and S. J. Pennycook, *Nano Energy*, 2018, **52**, 246-255.
54. J. Shuai, B. Ge, J. Mao, S. Song, Y. Wang and Z. Ren, *Journal of the American Chemical Society*, 2018, **140**, 1910-1915.
55. K. Imasato, S. Ohno, S. D. Kang and G. J. Snyder, *APL Materials*, 2018, **6**, 016106.
56. J. Shuai, J. Mao, S. Song, Q. Zhu, J. Sun, Y. Wang, R. He, J. Zhou, G. Chen and D. J. Singh, *Energy & Environmental Science*, 2017, **10**, 799-807.
57. J. Mao, J. Shuai, S. Song, Y. Wu, R. Dally, J. Zhou, Z. Liu, J. Sun, Q. Zhang and C. dela Cruz, *Proceedings of the National Academy of Sciences*, 2017, **114**, 10548-10553.
58. L. Akselrud and Y. Grin, *Journal of Applied Crystallography*, 2014, **47**, 803-805.
59. M. T. Agne, K. Imasato, S. Anand, K. Lee, S. K. Bux, A. Zevalkink, A. J. Rettie, D. Y. Chung, M. G. Kanatzidis and G. J. Snyder, *Materials Today Physics*, 2018, **6**, 83-88.
60. C. G. Maier and K. Kelley, *Journal of the American chemical society*, 1932, **54**, 3243-3246.
61. H.-S. Kim, Z. M. Gibbs, Y. Tang, H. Wang and G. J. Snyder, *APL materials*, 2015, **3**, 041506.
62. G. J. Snyder and A. H. Snyder, *Energy & Environmental Science*, 2017, **10**, 2280-2283.
63. K. Borup, J. de Boor, H. Wang, F. Drymiotis, F. Gascoin, X. Shi, L. Chen, M. Fedorov, E. Muller and B. Iversen, *Journal*.
64. H. Wang, W. D. Porter, H. Böttner, J. König, L. Chen, S. Bai, T. M. Tritt, A. Mayolet, J. Senawiratne and C. Smith, *Journal of electronic materials*, 2013, **42**, 654-664.
65. J. Xin, G. Li, G. Auffermann, H. Borrmann, W. Schnelle, J. Gooth, X. Zhao, T. Zhu, C. Felser and C. Fu, *Materials Today Physics*, 2018, **7**, 61-68.
66. K. Chua, *Nature*, 1968, **220**, 1317-1319.
67. J. Li, S. Zheng, T. Fang, L. Yue, S. Zhang and G. Lu, *Physical Chemistry Chemical Physics*, 2018, **20**, 7686-7693.
68. J. Zhang, L. Song, M. Sist, K. Tolborg and B. B. Iversen, *Nature communications*, 2018, **9**, 1-10.
69. K. Imasato, C. Fu, Y. Pan, M. Wood, J. J. Kuo, C. Felser and G. J. Snyder, *Advanced Materials*, 2020, **32**, 1908218.
70. F. Lv, Q. Zhang, W. Fan, X. Yang, J. Fan, H. Zhang, S. Chen, W. Wang and X. Tang, *Journal of materials science*, 2018, **53**, 8039-8048.
71. S. Song, J. Mao, J. Shuai, H. Zhu, Z. Ren, U. Saparamadu, Z. Tang, B. Wang and Z. Ren, *Applied Physics Letters*, 2018, **112**, 092103.
72. A. Bhardwaj, A. Rajput, A. Shukla, J. Pulikkotil, A. Srivastava, A. Dhar, G. Gupta, S. Auluck, D. Misra and R. Budhani, *RSC advances*, 2013, **3**, 8504-8516.
73. J. Li, S. Zhang, F. Jia, S. Zheng, X. Shi, D. Jiang, S. Wang, G. Lu, L. Wu and Z.-G. Chen, *Materials Today Physics*, 2020, **15**, 100269.
74. S. Song, J. Mao, M. Bordelon, R. He, Y. Wang, J. Shuai, J. Sun, X. Lei, Z. Ren and S. Chen, *Materials Today Physics*, 2019, **8**, 25-33.
75. Y. Wu, Z. Chen, P. Nan, F. Xiong, S. Lin, X. Zhang, Y. Chen, L. Chen, B. Ge and Y. Pei, *Joule*, 2019, **3**, 1276-1288.
76. Z. Liu, J. Mao, T.-H. Liu, G. Chen and Z. Ren, *MRS Bulletin*, 2018, **43**, 181-186.
77. G. J. Snyder, A. H. Snyder, M. Wood, R. Gurunathan, B. H. Snyder and C. Niu, *Advanced Materials*, 2020, 2001537.
78. W. Liu, J. Zhou, Q. Jie, Y. Li, H. S. Kim, J. Bao, G. Chen and Z. Ren, *Energy & Environmental Science*, 2016, **9**, 530-539.
79. I. T. Witting, J. A. Grovogui, V. P. Dravid and G. J. Snyder, *Journal of Materiomics*, 2020.

This journal is © The Royal Society of Chemistry 20xx

Please do not adjust margins

Thermoelectric

Melis Ozen, Mujde Yahyaoglu, Christophe Candolfi, Igor Veremchuk, Felix Kaiser, Ulrich Burkhardt, G. Jeffrey Snyder, Yuri Grin, and Umut Aydemir*

Enhanced Thermoelectric Performance in $Mg_{3+x}Sb_{1.5}Bi_{0.49}Te_{0.01}$ via Engineering Microstructure through Melt-Centrifugation

By applying the melt-centrifugation technique, porosity and dislocations are introduced in the microstructure of the *n*-type Zintl phase $Mg_{3+x}Sb_{1.5}Bi_{0.49}Te_{0.01}$leading to significantly low lattice thermal conductivity (κ_l ~0.33 W m^{-1} K^{-1} at 723 K) and enhanced thermoelectric efficiency (zT ~ 1.64 at 723 K). These results underline this lightweight material's strong potential to be used in mid-temperature thermoelectric power generation applications.